Micromechanics of $Ti_3C_2T_x$ MXene reinforced poly(vinyl alcohol) nanocomposites

Ming Dong , Yi Hu , Han Zhang , Emiliano Bilotti , Nicola Pugno , David Dunstan , Dimitrios G. Papageorgiou

PII: S2666-6820(23)00083-X
DOI: https://doi.org/10.1016/j.jcomc.2023.100427
Reference: JCOMC 100427

To appear in: *Composites Part C: Open Access*

Received date: 6 November 2023
Revised date: 3 December 2023
Accepted date: 13 December 2023

Please cite this article as: Ming Dong , Yi Hu , Han Zhang , Emiliano Bilotti , Nicola Pugno , David Dunstan , Dimitrios G. Papageorgiou , Micromechanics of $Ti_3C_2T_x$ MXene reinforced poly(vinyl alcohol) nanocomposites, *Composites Part C: Open Access* (2023), doi: https://doi.org/10.1016/j.jcomc.2023.100427

Micromechanics of $Ti_3C_2T_x$ MXene reinforced poly(vinyl alcohol) nanocomposites

Ming Dong[1*], Yi Hu[2,3], Han Zhang[2], Emiliano Bilotti[2,4], Nicola Pugno[2,5], David Dunstan[1], Dimitrios G. Papageorgiou[2*]

[1] *School of Physical and Chemical Sciences, Queen Mary University of London, London E1 4NS, United Kingdom*

[2] *School of Engineering and Materials Science, Queen Mary University of London, London E1 4NS, United Kingdom*

[3] *School of Mechanical Engineering, Northwestern Polytechnical University, Xi'an, 710072, PR China*

[4] *Department of Aeronautics, Imperial College London, South Kensington Campus, SW7 2AZ London, United Kingdom*

[5] *Laboratory for Bioinspired, Bionic, Nano, Meta Materials & Mechanics, Department for Civil, Environmental and Mechanical Engineering, University of Trento, Via Mesiano 77, Trento, 38123, Italy*

**Corresponding author's email: m.dong@qmul.ac.uk, d.papageorgiou@qmul.ac.uk*

Abstract

The key to effective mechanical reinforcement in polymer nancomposites lies within the stress transfer mechanisms and the distribution of the nanofillers within a polymer matrix. In this work, the micromechanics of $Ti_3C_2T_x$ MXene-reinforced poly(vinyl alcohol) (PVA) nanocomposites have been studied in detail. $Ti_3C_2T_x$ MXene/PVA nanocomposites were prepared by solution blending. The spatial orientation of $Ti_3C_2T_x$ MXene in the nanocomposites was characterized by polarized Raman spectroscopy and the orientation factor was correlated to the effective Young's modulus of the flakes through well-established micromechanical theories. The mechanical properties of the nanocomposites were evaluated by tensile testing. A 27% increase in Young's modulus and a 24% improvement in tensile strength were achieved by addition of only 0.6 wt% $Ti_3C_2T_x$. Efficient stress transfer from the polymer matrix to $Ti_3C_2T_x$ MXene in bulk nanocomposites has been observed through strain-induced Raman band shifts for the first time. The effective Young's modulus of the MXene nanoplatelets was calculated to be in the order of 300 GPa, in good agreement with the values derived from the application of micromechanical models.

1. Introduction

In recent years, two-dimensional (2D) materials such as graphene [1], hexagonal boron nitride [2], molybdenum disulfide (MoS_2) [3], MXenes [4] etc., have attracted huge research interest due to their unique combination of mechanical, thermal and electrical properties [5, 6]. Transition metal carbides and nitrides (MXenes) are 2D materials with a formula of $M_{n+1}X_nT_x$, where M is an early transition metal, X is carbon or nitrogen and T_x represents the functional groups on the surface of MXenes [7, 8]. MXenes were first synthesized from the Ti_3AlC_2 MAX phase by the Gogotsi group in 2011, using the hydrogen fluoride (HF) etching method [9]. Since then, more than 40 MXene compositions have been fabricated, making them one of the fastest growing 2D materials families [10]. The properties of MXenes can be adapted by tuning the ratio of M and X elements, ranging from M_2X to M_3X_2 and M_4X_3, thereby providing more opportunities to synthesize MXenes based on specific application demands [11, 12].

MXenes are excellent candidates for a wide range of applications, considering their electrochemical and optoelectronic properties. For example, MXenes possess metallic conductivity [13], high current breakdown density [14], and outstanding electrochemical properties [15]. MXenes also display promising performance towards energy storage and conversion [16, 17], catalysis [18, 19], electromagnetic interference shielding [20, 21], ultraviolet shielding [22], sensors [23, 24], electronics [25, 26], environment [27, 28], and biomedicine [29, 30].

Polymers are used extensively in our daily life due to their ease of processing, low cost, low density, satisfactory mechanical properties and good resistance to corrosion. High-performing nanofillers such as graphene and carbon nanotubes [31] have been extensively used as polymer reinforcements to overcome some of their intrinsic disadvantages such as the low thermal conductivity and high flammability, to further explore applications that demand multifunctionality [32, 33]. The exceptional intrinsic properties of MXene nanoplatelets make them suitable candidates for polymer reinforcement [34, 35]. Additionally, due to the presence of abundant

surface functional groups (-O, -OH, -F), MXenes display compatibility with water and organic solvents and can be incorporated into a variety of polymers through *ex situ* mixing or *in situ* polymerization [36]. Different interfacial interactions, such as hydrogen bonds [37], covalent bonds [38] and electrostatic interactions [39] can be formed between MXenes and polymer chains. Ling *et al.* [37] firstly explored the use of MXenes in polymer nanocomposites and fabricated MXene/polyvinyl alcohol (PVA) nanocomposites with high tensile strength (91 MPa, compared to 30 MPa for pure PVA), high electrical conductivity (240 S/cm) and notable volumetric capacitance (530 F/cm^3). After that, MXenes have been incorporated into many polymer matrices to fabricate nanocomposites for different applications (see review [36] and references within).

The mechanical properties of MXene-reinforced polymer composites play a vital role for structural and functional applications [40]. Experimentally, the Young's modulus of monolayer $Ti_3C_2T_x$ and $Nb_4C_3T_x$ was measured by atomic force microscopy (AFM) nanoindentation to be 333 ± 30 [41] and 386 ± 13 GPa [42], respectively, while theoretically (using molecular dynamics), the modulus of monolayer Ti_3C_2 was found almost equal to 502 GPa [43]. Quite interestingly, the in-plane stiffness and out-of-plane rigidity of MXenes increases with thickness and surface functionalization [44]. As a result, MXenes have been used as mechanical reinforcing agents in various polymers, such as epoxy resins [45, 46], ultrahigh-molecular-weight polyethylene (UHMWPE) [47], thermoplastic polyurethane (TPU) [48, 49] and natural rubber (NR) [50]. With the addition of 0.5 wt% Ti_3C_2, the tensile strength and storage modulus of a Ti_3C_2/TPU film increased by 47.1% and 39.8%, respectively [48]. In another study, methyltetrahydrophthalic anhydride (MTHPA) was used to facilitate the dispersion of $Ti_3C_2T_x$ in an epoxy resin and the formation of robust interfaces with the epoxy [45]. The elastic modulus and tensile strength were increased by 31 % (from 2.6 to 3.5 GPa) and 51 % (from 70.5 to 106.4 MPa) with only 0.2 wt% $Ti_3C_2T_x$. These studies demonstrate that mechanical reinforcement can be achieved by using MXenes even at low filler contents. However, the mechanisms of polymer reinforcement from

MXenes (e.g. the stress transfer mechanism) and the spatial orientation of MXenes within a polymer matrix have not been examined thoroughly yet.

Raman spectroscopy has been widely used to study stress transfer mechanisms in polymer nanocomposites reinforced by nanomaterials [51, 52]. The applied stress can induce changes in bond length and a subsequent shift is recorded in the characteristic Raman bands [53]. Therefore, stress transfer can be analysed by monitoring the shift of Raman peaks. For nanocarbon-reinforced nanocomposites (such as carbon nanotubes (CNTs) [54], graphene nanoplatelets (GNPs) [52] and graphene oxide (GO) [55]), the G or 2D Raman bands have been used to gain an insight into the micromechanics of composites. This technique has been extended to other nanofillers beyond carbon nanomaterials such as tungsten disulfide (WS_2) [56] and hexagonal boron nitride (hBN) [57]. In a recent study, the interfacial stress transfer from a polymer matrix (PMMA) to $Ti_3C_2T_x$ flakes was investigated by strain-induced Raman band shifts in a model nanocomposite configuration (where a $Ti_3C_2T_x$ flake was coated with a polymer layer) [58]. It was shown that MXenes with a length of 10 μm and a thickness of tens of nanometers can provide efficient mechanical reinforcement to a polymer matrix. However, Raman spectroscopy has not been used yet to gain insights into the stress transfer mechanisms in bulk MXene/polymer nanocomposites.

In this study, Raman spectroscopy was used to quantify the spatial orientation and follow the deformation of $Ti_3C_2T_x$ MXene within a poly(vinyl alcohol) matrix. The $Ti_3C_2T_x$ MXene/PVA nanocomposites were prepared by solution casting and were characterized by X-ray diffraction, tensile testing and Raman spectroscopy. From the use of micromechanical theories and the evaluation of strain-induced Raman band shifts, the efficiency of mechanical reinforcement by $Ti_3C_2T_x$ MXene was investigated in detail and is presented in the following sections.

2. Experimental section

2.1 Materials

Ti_3AlC_2 MAX powders (particle size of 38 μm, purity of 98%) were obtained from Jilin 11 Technology Co., Ltd. Lithium fluoride (LiF, 98.5% grade) powder and hydrochloric acid (HCl, ACS reagent) were purchased from Sigma-Aldrich. The PVA powder with an average molecular weight of 67,000 g/mol and degree of hydrolysis of 88% was provided by ME Scientific Engineering Ltd.

2.2 Synthesis of $Ti_3C_2T_x$ MXene nanoplatelets

The $Ti_3C_2T_x$ MXene nanoplatelets were prepared by the HF etching method [59] as illustrated in Figure 1a. First, 1.6 g LiF was slowly dissolved in 20 ml 9 M HCl in a beaker and left under magnetic stirring for 30 min to prepare the etchant. Then, a total of 1 g Ti_3AlC_2 MAX powder was gradually added to the prepared etchant and the reaction was kept at 40 ˚C for 24 h under continuous stirring. The mixture was subsequently washed with deionized water via centrifugation at 3500 rpm for 5 min per cycle until the pH of the supernatant reached 6−7. The sediment was then collected and redispersed in DI water to start the delamination process. The mixture was mildly sonicated (60 W) for 10 min in an ice bath under Ar flow. Finally, the mixture was centrifuged at 3500 rpm for 20 min to obtain the MXene suspension. The concentration of the obtained MXene suspension was determined by vacuum filtering of a certain amount of suspension through a mixed cellulose ester (MCE) membrane with pore size of 0.22 μm. A filtered MXene film is shown in Figure S1 and the concentration of the suspension was about 3 mg/ml.

2.3 Preparation of $Ti_3C_2T_x$ MXene/PVA nanocomposites

The fabrication of $Ti_3C_2T_x$ MXene/PVA nanocomposites is presented schematically in Figure 1b. The PVA powder was initially dissolved in DI water at 90 ℃ to produce a 5 wt% PVA aqueous solution. Then, the MXene suspension and the PVA solution were mixed to prepare

nanocomposites with the desired MXene weight content (0.3, 0.6, 0.9 and 1.2 wt%). The mixtures were left under magnetic stirring for about 1h at room temperature to obtain homogeneous dispersions. For mechanical testing, the $Ti_3C_2T_x$ MXene/PVA films were prepared by pouring the mixtures into petri dishes and drying at 60 ℃ for 24 h. For Raman measurements, 20 µl of the MXene/PVA mixture were drop cast on top of a PMMA beam and dried at 60 ℃ for 24 h.

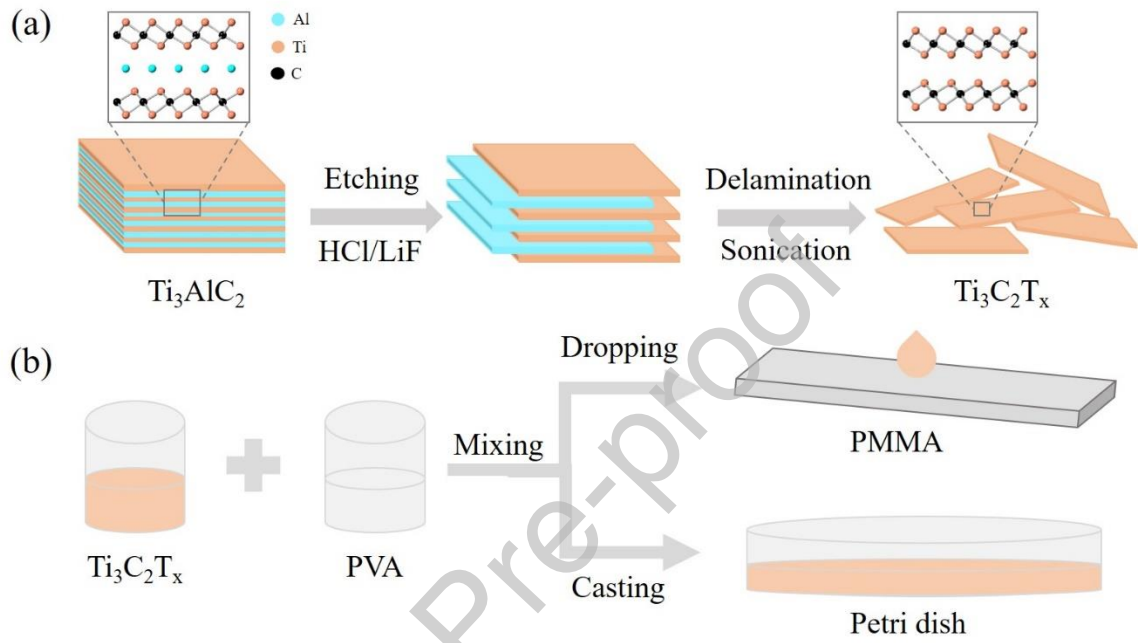

Figure 1. (a) Liquid exfoliation of MAX Ti_3AlC_2 to MXene $Ti_3C_2T_x$. (b) Preparation of $Ti_3C_2T_x$ /PVA nanocomposites. For the samples that were examined by *in situ* Raman tests, small amounts of the mixtures were dropped onto a PMMA beam; for the samples that were used for tensile tests, the mixtures were cast into a Petri dish.

2.4 Characterizations

2.4.1 X-ray diffraction

X-ray diffraction (XRD) was carried out using an Analytical X'Pert-Pro diffractometer with a Cu-Kα radiation source. The scan was operated in 2θ geometry at the range of 5-70˚ in reflection mode.

2.4.2 Atomic force microscopy

Atomic force microscopy (AFM) was performed in semi-contact mode to study the morphology and thickness of exfoliated $Ti_3C_2T_x$ flakes. The samples were prepared by depositing $Ti_3C_2T_x$ diluted in DI water onto a silicon substrate and the mixture was then dried at room temperature. AFM tips with a spring constant of 42 N/m and resonant frequency of 350 kHz were used.

2.4.3 Scanning electron microscopy

The microstructure of both exfoliated MXenes and cryofractured composite samples (after immersion in liquid N_2) was observed using scanning electron microscopy (SEM, FEI Inspect-F, Netherlands) with an acceleration voltage of 5 kV.

2.4.4 Fourier transform infrared spectroscopy

Fourier transform infrared (FTIR) spectroscopy was used to study the functional groups of $Ti_3C_2T_x$ MXene (Bruker Tensor 27). The scanning range was 4000–1000 cm^{-1} and the resolution was 4 cm^{-1}.

2.4.5 Differential scanning calorimetry

Differential scanning calorimetry (DSC) measurements of the composite films were conducted with a TA DSC 25 under an argon flow of 20 ml/min. The sample was heated at a rate of 10 ^{o}C/min from 10 to 280 ℃. The sample was held at 280 ^{o}C for 5 mins to erase the thermal history, cooled down to room temperature at 50 ^{o}C/min and then reheated at 10 ^{o}C/min to record the melting point.

2.4.6 Mechanical testing

The tensile properties of pure PVA and $Ti_3C_2T_x$/PVA nanocomposites at different loadings were studied using an Instron 5900R84. The films were cut into dogbone specimens with a gauge length of 10 mm and a width of 3 mm. The thickness of the samples was about 0.05 ± 0.01 mm. For each $Ti_3C_2T_x$/PVA nanocomposite, five samples were tested. The load cell was 100 N and the loading rate was 1 mm/min.

2.4.7 Raman spectroscopy

Raman spectroscopy data were collected using a micro-Raman spectrometer (Renishaw inVia) in a backscattering configuration. A laser excitation of 785 nm with a grating of 1200 grooves/mm was used to record the Raman signal. The laser power was kept below 1 mW to avoid laser heating effects. The exposure time was 10 s for each measurement.

Polarized Raman spectroscopy was used to determine the orientation of the MXene flakes in the polymer matrix. The VV (vertical/vertical) polarization, where the incident and scattered polarization were the same, was selected. The set-up of polarized Raman spectroscopy is illustrated in Figure S3. The $Ti_3C_2T_x$/PVA samples were placed on a rotation stage, and the laser beam was parallel to *z* and *x* directions respectively. The stage was rotated in steps of 10˚.

For the *in situ* Raman deformation study, a four-point bending device was adjusted on the microscope stage. A strain gauge was attached to the centre of the beam to monitor the strain. The strain was applied to the specimen in steps of about 0.05%. Three spectra were recorded and then averaged at each strain level.

3. Results and discussion

3.1 Microstructure of $Ti_3C_2T_x$ MXene nanoplatelets

The XRD patterns of Ti_3AlC_2 MAX and $Ti_3C_2T_x$ MXene are shown in Figure 2a. It can be seen that Ti_3AlC_2 shows the main characteristic peak from the (104) reflection at 2θ=38.9˚, corresponding to the presence of the Al element. This peak is not observed in $Ti_3C_2T_x$ MXene, which means that the Al layer was fully etched after the *in situ* HF etching method [59]. Meanwhile, the (002) peak of Ti_3AlC_2 at 9.59˚ moved to 7.12˚ for $Ti_3C_2T_x$. This indicates that the d-spacing increased from 0.92 nm to 1.24 nm due to the presence of Li^+. In addition, four more minor peaks corresponding to reflections from (004), (006), (008) and (010) crystal planes were also observed for $Ti_3C_2T_x$.

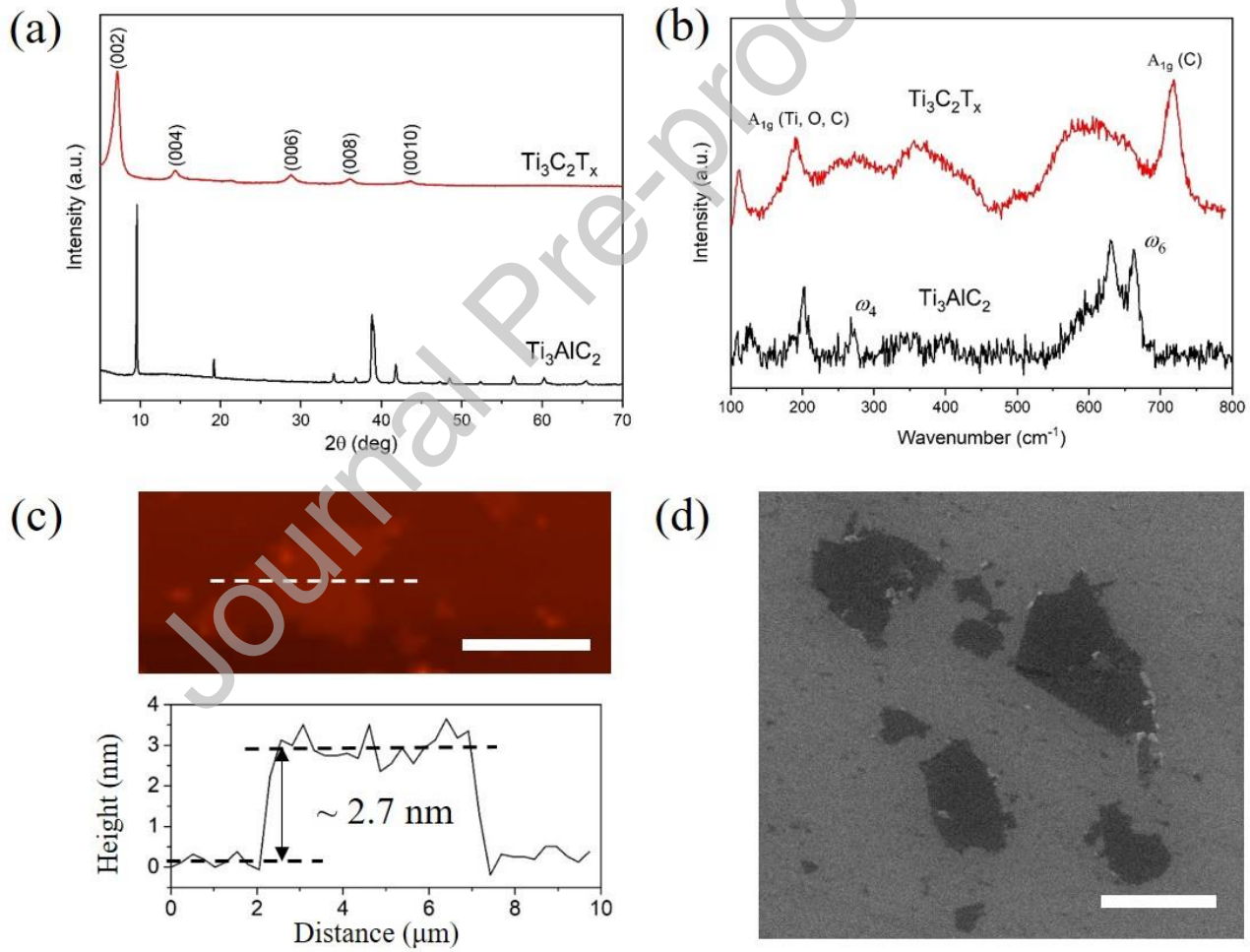

Figure 2. (a) XRD patterns of Ti_3AlC_2 MAX and $Ti_3C_2T_x$ MXene. (b) Raman spectrum of Ti_3AlC_2 MAX and $Ti_3C_2T_x$ MXene. (c) AFM image of exfoliated $Ti_3C_2T_x$ nanosheet. Scale bar, 5 μm. (d) SEM image of exfoliated $Ti_3C_2T_x$ nanosheet. Scale bar, 2.5 μm.

The Raman spectra of Ti_3AlC_2 and $Ti_3C_2T_x$ are shown in Figure 2b. The feature peaks of both Ti_3AlC_2 and $Ti_3C_2T_x$ lie in the 100−800 cm^{-1} range. The out-of-plane A_{1g} (Ti, Al) peak, ω_4, of Ti_3AlC_2 MAX moved to lower wavenumber for $Ti_3C_2T_x$ MXene (A_{1g} (Ti, O, C) in Figure 2b) as Al was etched away and C and surface groups were involved in vibration [60]. Additionally, another out-of-plane peak of Ti_3AlC_2 (ω_6) moved to higher wavenumber in the case of $Ti_3C_2T_x$ (A_{1g} (C) in Figure 2b). Overall, both out-of-plane vibration modes of Ti_3AlC_2 shifted due to the etching of Al and the effective exfoliation of the MXene nanoplatelets.

The morphologies of the exfoliated flakes were characterized by AFM and SEM. An AFM image of an exfoliated $Ti_3C_2T_x$ flake deposited on a silicon substrate is shown in Figure 2c. The height of the flake is about 2.7 nm, corresponding to a monolayer sample [61]. The lateral size of the flake is about 5 μm, which is an indication that relatively large flakes have been mostly obtained due to the use of mild sonication, even though tiny fragments can also be seen that contribute less towards mechanical reinforcement. Figure 1d is an SEM image of exfoliated $Ti_3C_2T_x$ flakes. The flakes mainly display smooth and flat surfaces, evidencing that topological undulations such as wrinkles or folds were not introduced by etching and sonication. Finally, the functional groups on the surface of $Ti_3C_2T_x$ MXene nanoplatelets were studied by FTIR spectroscopy, as shown in Figure S2 (Supporting Information). The peaks at 3428 and 1627 cm^{-1} can be assigned to the stretching vibration of hydrogen bonded hydroxyl (–OH) group and the bending vibration of C–OH bond, respectively [62].

3.2 Orientation of $Ti_3C_2T_x$ in PVA matrix

The XRD patterns of pure PVA and the $Ti_3C_2T_x$/PVA films with various loadings are shown in Figure 3a. There is no obvious difference between the diffraction patterns of pure PVA and $Ti_3C_2T_x$/PVA composites, and all the samples show a peak at $2\theta = 19.6^{\circ}$ representing reflections from (101) plane of PVA [63]. The intensity and position of the main XRD peak was similar for all samples, an indication that degree of crystallinity, the size of PVA crystals and the orientation of PVA macromolecular chains did not change significantly with increasing $Ti_3C_2T_x$ loading. The characteristic peaks of pure $Ti_3C_2T_x$ (illustrated in Figure 1a) are not observed in the composite films, an indication that the $Ti_3C_2T_x$ flakes were exfoliated in the PVA matrix.

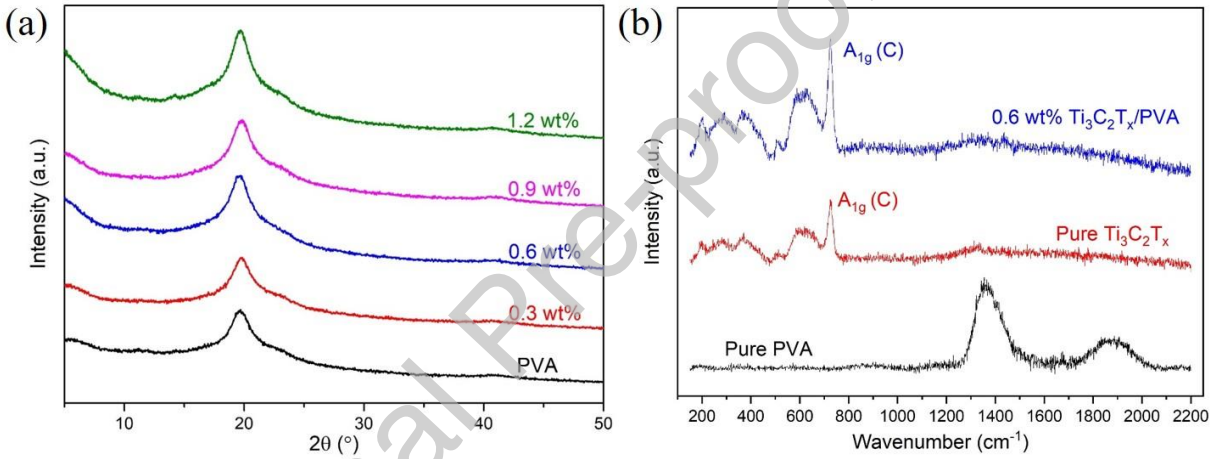

Figure 3. (a) XRD patterns of pure PVA and $Ti_3C_2T_x$/PVA films with different filler loadings. (b) Raman spectrum of pure PVA, pure $Ti_3C_2T_x$ and 0.6 wt% $Ti_3C_2T_x$/PVA film.

Figure 3b compares the Raman spectra of PVA, $Ti_3C_2T_x$ and $Ti_3C_2T_x$/PVA film from 150 to 2200 cm^{-1}. In contrast to the XRD patterns, the Raman spectrum of $Ti_3C_2T_x$/PVA film is dominated by the $Ti_3C_2T_x$ modes despite the low loading of the filler. $Ti_3C_2T_x$ is in resonance when the 785 nm laser is used and therefore the intensity of Raman bands is high [60]. The important work of Hu *et al.* [64] can serve as a useful reference towards the structural and vibrational analysis of bare Ti_3C_2 and T-terminated $Ti_3C_2T_2$ MXenes using Raman spectroscopy. The A_{1g} (C) peak of $Ti_3C_2T_x$

originating from the out-of-plane vibration of carbon atoms is intense and sharp; therefore, this peak was used for the analysis of orientation and strain-induced band shifts.

Polarized Raman spectroscopy was used to characterize the orientation of $Ti_3C_2T_x$ flakes in the PVA matrix. Polar plots of the normalized A_{1g} intensity for the 0.6 wt% $Ti_3C_2T_x$/PVA film with the laser parallel to the *z* and *x* directions are presented in Figure 4. When the laser is parallel to the *z* direction, the intensity of the A_{1g} peak is independent of the rotation angle and is almost constant (Figure 4a). The red solid line is the fitting curve using $I_{A1g} = 1$, indicating that $Ti_3C_2T_x$ is isotropic in the *z* axis. Therefore, the results obtained when the laser is parallel to the *x* direction will be able to describe the spatial orientation of $Ti_3C_2T_x$ in the matrix [65]. In that case, the intensity of A_{1g} peak shows a regular variation as a function of rotation angle, as illustrated in Figure 4b. Similar results have been reported for the spatial orientation of GO in PVA using the D band [65] and GNPs in thermoplastic elastomers using the G band [66]. The following relationship was used to fit the data by using the polar coordinates of the *z* direction θ and Φ [67]

$$I(\Phi) = I_o \left\{ \frac{8}{15} + \langle P_2(\cos\theta)\rangle \left(-\frac{16}{21} + \frac{8}{7}\cos^2\Phi \right) + \langle P_4(\cos\theta)\rangle \left(\frac{8}{35} - \frac{8}{7}\cos^2\Phi + \cos^4\Phi \right) \right\}, \quad (1)$$

where I_o is the amplitude and $\langle P_2(\cos\theta)\rangle$ and $\langle P_4(\cos\theta)\rangle$ are fitting parameters that enable quantification of the spatial orientation of flakes in matrix [65]. These two parameters can be correlated to the Krenchel orientation factor, η_o, as

$$\eta_o = \frac{8}{15} + \frac{8}{21}\langle P_2(\cos\theta)\rangle + \frac{3}{35}\langle P_4(\cos\theta)\rangle, \quad (2)$$

where η_o is equal to 0.53 for random orientation of 2D materials within a polymer matrix and is equal to 1 for in-plane orientation [31].

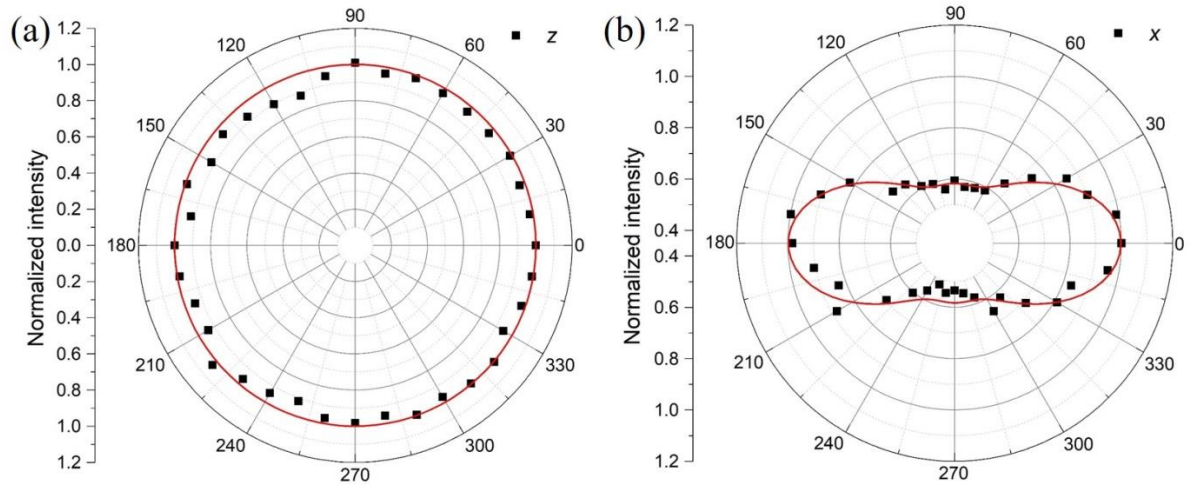

Figure 4. Variation of the normalized intensity of A_{1g} peak with rotation angle using VV polarization when the laser is parallel to (a) *z*-axis and (b) *x-axis*, respectively. The filler loading is 0.6 wt%. The black dots represent experimental results and the red lines represent fitting results with (a) $I_{A1g} = 1$ and (b) $\langle P_2(\cos\theta)\rangle = 0.28$ and $\langle P_4(\cos\theta)\rangle = 0.30$.

For the fitting of experimental data in Figure 4b, the parameters $\langle P_2(\cos\theta)\rangle = 0.28$ and $\langle P_4(\cos\theta)\rangle = 0.30$ were used. The results for all composites at different filler loadings are presented in Figure S4 and summarized in Table 1. There is no preferred orientation in the *z* direction, while the samples display a preferential in-plane (*x*-*y*) orientation as a result of the solution casting process. By substituting the $\langle P_2(\cos\theta)\rangle$ and $\langle P_4(\cos\theta)\rangle$ values into Equation 2, the orientation factor (η_0) can be determined. The orientation factors are similar at different filler loadings with values varying between 0.65 and 0.67. These values are slightly lower than the in-plane orientation of the previously reported GO sheets in a PVA matrix (0.69 to 0.78), with considerably higher filler loadings [65]. Given the fact that oriented fillers along the tensile direction contribute significantly towards mechanical reinforcement, it is anticipated that the mechanical properties of the MXene nanocomposites should be considerably improved even at low filler contents.

Table 1. Values of $\langle P_2(\cos\theta)\rangle$, $\langle P_4(\cos\theta)\rangle$ and η_o determined for measurements where the laser beam was parallel to the *x* direction of the sample surfaces.

Samples	Filler content (wt%)	$\langle P_2(\cos\theta)\rangle$	$\langle P_4(\cos\theta)\rangle$	η_o
PVA/$Ti_3C_2T_x$	0.3	0.27	0.31	0.66
	0.6	0.28	0.30	0.67
	0.9	0.25	0.30	0.65
	1.2	0.26	0.28	0.66

3.3 Mechanical properties of $Ti_3C_2T_x$/PVA films

The mechanical properties of pure PVA and $Ti_3C_2T_x$/PVA nanocomposite films were characterized by tensile testing. Typical stress-strain curves of pure PVA and the 0.6 wt% $Ti_3C_2T_x$/PVA nanocomposite are presented in Figure 5a. The elastic region of the stress-strain curves and the determination of Young's modulus is shown in Figure S5 in Supporting Information. The Young's modulus and tensile strength of the composites increased (Figure 5b) while the elongation at break decreased with increasing $Ti_3C_2T_x$. At 0.6 wt% $Ti_3C_2T_x$, the Young's modulus of pure PVA (2.21 GPa) increased by 27% to 2.81 GPa. Beyond this concentration, the Young's modulus remained almost constant. The tensile strength improved by 24% from 68.3 to 84.9 MPa with 0.6 wt% $Ti_3C_2T_x$; however the tensile strength decreased with larger filler loading. Given that the tensile strength is more sensitive to defects and aggregation, this might be an indication that agglomerates were formed at nanocomposite loadings higher than 0.6 wt%. The SEM images taken from cryofractured samples reveal a homogeneous distribution of fillers at low contents (Fig 6a,b) which allows for efficient reinforcement, while at higher filler contents (Fig 6c,d) some aggregated regions can be seen, known to act as stress concentration points during the application of strain. It is important to notice that the MXenes appear well-wetted by the polymer matrix, ensuring that stress is transferred effectively from the matrix to the fillers. A certain degree of orientation can be also observed in all SEM images as a result of the casting process that was used to prepare the MXene

nanocomposites; the degree of orientation has already been quantified through polarized Raman spectroscopy and presented in Section 3.2.

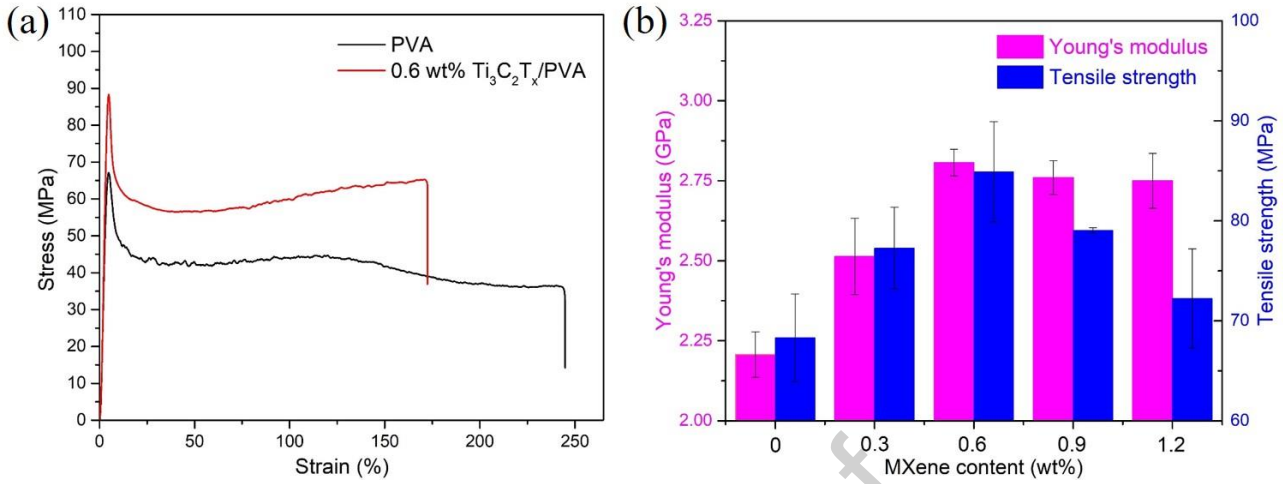

Figure 5. (a) Stress-strain curves of pure PVA and 0.6 wt% $Ti_3C_2T_x$/PVA. (b) Young's modulus (pink bars) and tensile strength (blue bars) of pure PVA and $Ti_3C_2T_x$/PVA nanocomposites with different filler loadings (0.3, 0.6, 0.9 and 1.2 wt%).

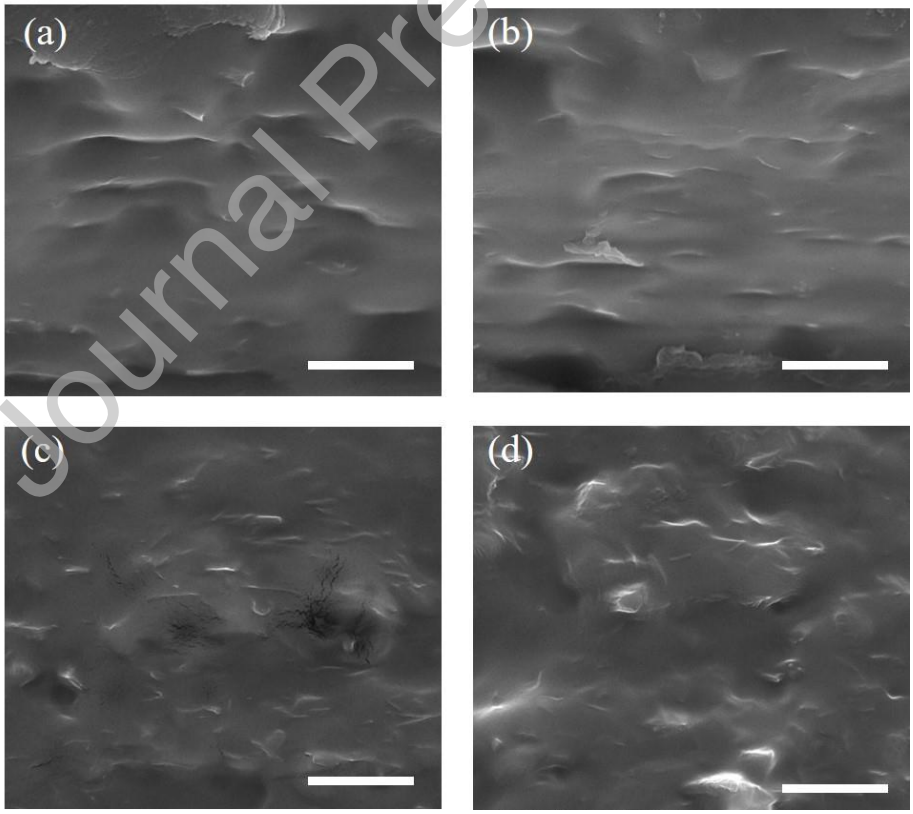

Figure 6. SEM images of cryofractured PVA/MXene nanocomposites at (a) 0.3, (b) 0.6, (c) 0.9 and (d) 1.2 wt% filler contents. Scale bars, 2.5 μm.

The mechanical properties of polymers and their nanocomposites can be also associated with changes in the degree of crystallinity of the matrix. The degree of crystallinity of PVA and its nanocomposites, as derived from DSC curves (Figure S6) is presented in Table S1. The incorporation of $Ti_3C_2T_x$ did not change the crystallinity significantly. As a result, the changes in the mechanical properties cannot be attributed to changes in crystallinity but to the presence of the MXene nanofillers, their degree of orientation and ultimately, the formation of a strong polymer-filler interface.

3.4 Strain-induced Raman band shifts

The mechanics of filler reinforcement can be studied through the evaluation of the stress transfer mechanism at the polymer-filler interface [52]. In a previous study, the shift rate of Raman A_{1g} mode with strain was used to study the deformation and interfacial stress transfer in model Ti_3C_2 polymer nanocomposites [58]. Raman spectra with the laser beam parallel to the *z* axis were collected from $Ti_3C_2T_x$/PVA nanocomposites and the position of the A_{1g} mode was recorded as a function of strain. Figure 7 shows the A_{1g} peak of 0.6 wt% $Ti_3C_2T_x$/PVA nanocomposite at 0 and 0.4 % strain. There is a downshift of the position of the A_{1g} peak as the stress was transferred from the PVA matrix to the flake. The peaks were fitted by a single Lorentzian function (Figure S7). At 0.4 % applied strain, the peak undergoes a downshift of about 1.1 cm^{-1}.

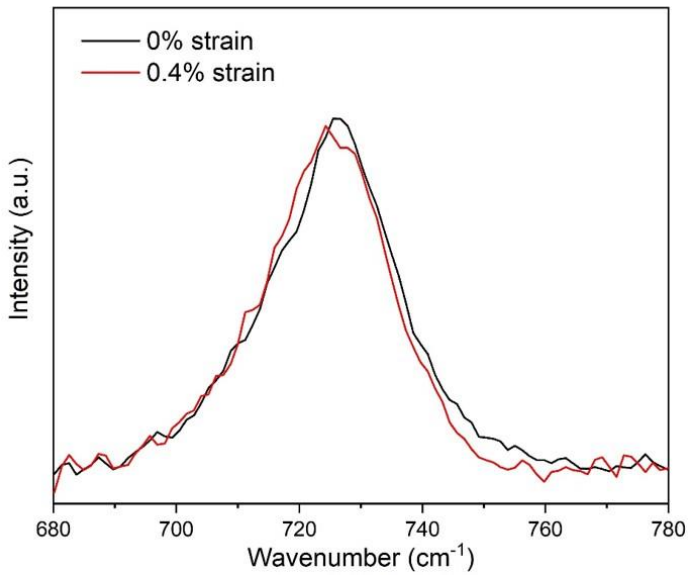

Figure 7. Raman A_{1g} band of 0.6 wt% $Ti_3C_2T_x$/PVA nanocomposite before (0% strain) and after (0.4% strain) tensile deformation.

Figure 8 shows the position of Raman A_{1g} band as a function of strain measured for the $Ti_3C_2T_x$/PVA nanocomposites. There is a linear downshift in A_{1g} band position with the increase of strain until 0.45% strain for all the samples. This redshift indicates an effective stress transfer from PVA to $Ti_3C_2T_x$ flakes and the presence of a strong polymer-filler interface [68]. After that, there is no further shift in the characteristic Raman A_{1g} band which is probably induced by failure of the interface and slippage between PVA and $Ti_3C_2T_x$ [57]. The band shifts were fitted with straight lines and the slopes were obtained for all the samples. For the 0.3 wt% $Ti_3C_2T_x$/PVA nanocomposite, a slope of -2.8 ± 0.1 cm^{-1}/% was observed as shown in Figure 8a. This value is slightly lower than the value of $Ti_3C_2T_x$ flake deposited on a PMMA beam (-3.7 cm^{-1}/%) [58]. This is reasonable as in our case the flakes were dispersed in a bulk polymer matrix and the orientation of the flakes was not perfectly parallel to the strain direction. Therefore, the flakes were not fully stretched along the in-plane direction. A slope of -2.7 ± 0.2 cm^{-1}/% was derived for the 0.6 wt% $Ti_3C_2T_x$/PVA nanocomposite as shown in Figure 8b, which is similar to the case of the sample filled with 0.3 wt% $Ti_3C_2T_x$. When the filler content increases to 0.9 wt%, a poorer stress transfer

efficiency can be deduced from the decrease of the slope of A_{1g} band position to -1.5 ± 0.1 cm^{-1}/%. The slope further decreased to -1.2 ± 0.1 cm^{-1}/% with 1.2 wt% $Ti_3C_2T_x$ filler loading. These are indications of a slight aggregation of the MXene nanoparticles, even though the loadings can be considered quite small. To avoid sample-to-sample variation, two more samples were studied for each loading and the results are illustrated in Figure S8, clearly showing that variation between samples was small. The derived slopes of Raman band shifts can be used to determine the effective Young's modulus of the filler as presented in the next section.

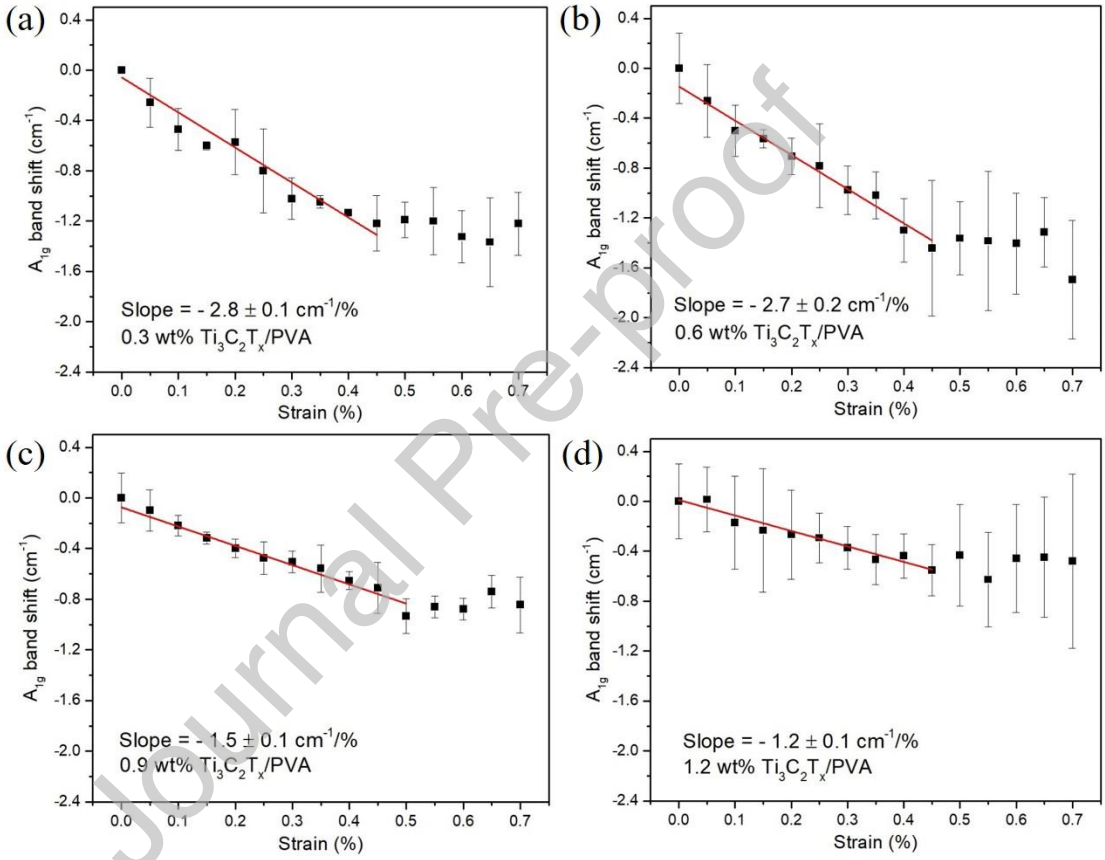

Figure 8. Strain-induced Raman A_{1g} band shifts of $Ti_3C_2T_x$/PVA nanocomposites at (a) 0.3, (b) 0.6, (c) 0.9 and (d) 1.2 wt% filler contents.

3.5 Micromechanics of reinforcement

The mechanics of reinforcement of a low-modulus matrix with a high-modulus filler under uniform strain can be described by the well-established modified rule of mixtures (mRoM) [69]. According to the theory, the Young's modulus of a composite, E_c, is given by

$$E_c = E_{eff} V_f + E_m (1 - V_f), \quad (3)$$

where E_{eff} is the effective Young's modulus of the nanofiller, E_m is the Young's modulus of the matrix, and V_f is the volume fraction of the nanofiller. The conversion of wt% to vol% is presented in Supporting Information – S9. The density of $Ti_3C_2T_x$ is 4.21 g/cm^3 and the density of PVA is 1.3 g/cm^3 [57]. The weight fractions of 0.3, 0.6, 0.9 and 1.2 wt% correspond to volume fractions of 0.09, 0.19, 0.28 and 0.37 vol%, respectively.

By substituting the volume fractions and the Young's modulus of the matrix and nanocomposites (listed in Table 2) into Equation 3, the effective Young's modulus of $Ti_3C_2T_x$ nanoplatelets was calculated and summarized in Table 2. The E_{eff} of $Ti_3C_2T_x$ is about 342.9 and 318.0 GPa for 0.3 wt% and 0.6 wt% loadings, respectively, and reduces to 199.8 GPa at 0.9 wt% and 149.1 GPa at 1.2 wt%. The dependence of E_c upon V_f for the nanocomposites is shown in Figure S9. There is an approximately linear increase in composite modulus with volume fraction until 0.6 wt%. From the initial slope of the curve, the value of E_{eff} for $Ti_3C_2T_x$ was determined to be 314.4 GPa, which is close to the values determined using Equation 3 for the nanocomposites with 0.3 and 0.6 wt% filler content.

Table 2. Mechanical properties of PVA/$Ti_3C_2T_x$ nanocomposites and filler modulus determined from mechanical testing and Raman band shifts.

Samples	Filler content (wt%, vol%)	Young's modulus (GPa)	E_{eff} (GPa) (Mechanical)	η_l	$d\omega_{A1g}/d\varepsilon$ (cm^{-1}/%)	E_R (GPa) (Raman)
PVA	0, 0	2.21 ± 0.07	–	–	–	–
PVA/$Ti_3C_2T_x$	0.3, 0.09	2.51 ± 0.12	342.9	1	2.7 ± 0.1	366.3
	0.6, 0.19	2.81 ± 0.04	318.0	0.95	2.7 ± 0.1	366.3

0.9, 0.28	2.76 ± 0.05	199.8	0.61	1.5 ± 0.1	203.5
1.2, 0.37	2.75 ± 0.09	149.1	0.45	1.3 ± 0.1	176.4

The effective Young's modulus of MXene flakes can also be estimated independently from the Raman band shift rates upon strain (E_R). The shift rates of A_{1g} band derived in Section 3.4 can be used to determine the value of E_R as

$$E_R = \frac{d\omega_{A_{1g}}}{d\varepsilon} \frac{E_f}{\left(d\omega_{A_{1g}}/d\varepsilon\right)_{ref}} \text{GPa}, \quad (4)$$

where $d\omega_{A_{1g}}/d\varepsilon$ is the shift rate of $Ti_3C_2T_x$ Raman A_{1g} mode with strain, the reference shift rate value is taken as -3.7 cm^{-1}/%, and E_f is the intrinsic Young's modulus of monolayer $Ti_3C_2T_x$. Here, the E_f value of 502 GPa (Ti_3C_2) was used [43], as it has been shown that the Young's modulus of $Ti_3C_2T_x$ is similar with the value of Ti_3C_2 [44]. The values of the effective Young's modulus of $Ti_3C_2T_x$ as determined from Raman band shifts are listed in Table 2. It can be seen that E_R is generally higher than E_{eff}. Similar behaviour has been observed in a number of polymers reinforced by GNPs and can be attributed to a higher degree of orientation and possibly a higher aspect ratio of the individual flakes that have been studied by Raman spectroscopy [52].

The determination of the effective Young's modulus allows the mechanical reinforcing efficiency to be evaluated. If we take the effect of orientation and finite length of flakes into account, the effective Young's modulus can be given as [57]

$$E_{eff} = \eta_l \eta_o E_f, \quad (5)$$

where E_f is the Young's modulus of the flake, η_o is the Krenchel orientation factor that was calculated in Section 3.2 and η_l is the length factor that takes values between 0 (for no stress transfer) and 1 (for perfect stress transfer). The length factor reflects the stress transfer efficiency from the matrix to the filler which is not only dependent on the shape of the filler but also on the interfacial strength between the filler and the matrix; therefore its determination is critical towards understanding the micromechanics of reinforcement [52]. If we use the effective Young's modulus

from mechanical testing and the orientation factor from Raman spectra (Table 1), the length factor can be calculated. The results are summarized in Table 2. It can be seen that the length factor is close to 1 at 0.3 and 0.6 wt% filler loadings, indicating effective stress transfer from the matrix to the MXenes at low loadings. With further increase in filler loading, the length factor was degraded, dropping to 0.61 at 0.9 wt% and 0.45 at 1.2 wt%. This is consistent with the stress-induced Raman band shifts as stated above. The slight aggregation of the MXene nanoparticles at 0.9 and 1.2 wt% leads to a deterioration of the stress transfer from the matrix to the filler which is also reflected in the reduction of the length factor.

4. Conclusions

The introduction of $Ti_3C_2T_x$ flakes in a PVA matrix leads to an improvement of mechanical properties. A new insight into the micromechanics of reinforcement of $Ti_3C_2T_x$ MXene within the PVA matrix was provided using Raman spectroscopy. Specifically, the spatial distribution of $Ti_3C_2T_x$ in PVA was characterized by polarized Raman spectroscopy and the Krenchel orientation factor was determined quantitatively. The results revealed that nanoplatelets displayed a certain degree of in-plane orientation, which allows for effective reinforcement along the tensile direction. The interfacial interactions were evaluated by strain-induced Raman band shifts for all nanocomposites under study. This allowed the calculation of the effective Young's modulus of $Ti_3C_2T_x$ which showed good agreement with the values derived from mechanical testing. The effective Young's modulus of MXene nanoplatelets was in the order of 300 GPa at low filler contents, revealing the great potential of the filler towards mechanical reinforcement of bulk polymers in a number of applications, once MXene scalability and fabrication issues are resolved. Lastly, this work revealed once again the wealth of information that can be exported through the use of Raman spectroscopy in strong resonance systems such as 2D materials- reinforced polymer nanocomposites.

Conflicts of interest

There are no conflicts to declare.

Acknowledgement

M. Dong acknowledges support from the China Scholarship Council (CSC). The authors acknowledge the support from "Graphene Core 3" GA: 881603 which is implemented under the EU-Horizon 2020 Research & Innovation Actions (RIA) and is financially supported by EC-financed parts of the Graphene Flagship.

References

[1] Novoselov KS, Geim AK, Morozov SV, Jiang D, Zhang Y, Dubonos SV, et al. Electric field effect in atomically thin carbon films. Science. 2004;306:666-9.
[2] Weng QH, Wang XB, Wang X, Bando Y, Golberg D. Functionalized hexagonal boron nitride nanomaterials: emerging properties and applications. Chem Soc Rev. 2016;45:3989-4012.
[3] Li X, Zhu HW. Two-dimensional MoS2: Properties, preparation, and applications. J Materiomics. 2015;1:33-44.
[4] Naguib M, Mochalin VN, Barsoum MW, Gogotsi Y. 25th Anniversary Article: MXenes: A New Family of Two-Dimensional Materials. Adv Mater. 2014;26:992-1005.
[5] Zhao MT, Lu QP, Ma QL, Zhang H. Two-Dimensional Metal-Organic Framework Nanosheets. Small Methods. 2017;1:8.
[6] Ferrari AC, Bonaccorso F, Fal'ko V, Novoselov KS, Roche S, Boggild P, et al. Science and technology roadmap for graphene, related two-dimensional crystals, and hybrid systems. Nanoscale. 2015;7:4598-810.
[7] Mohammadi AV, Rosen J, Gogotsi Y. The world of two-dimensional carbides and nitrides (MXenes). Science. 2021;372:1165-+.
[8] Shekhirev M, Shuck CE, Sarycheva A, Gogotsi Y. Characterization of MXenes at every step, from their precursors to single flakes and assembled films. Prog Mater Sci. 2021;120:31.
[9] Naguib M, Kurtoglu M, Presser V, Lu J, Niu JJ, Heon M, et al. Two-Dimensional Nanocrystals Produced by Exfoliation of Ti_3AlC_2. Adv Mater. 2011;23:4248-53.
[10] Naguib M, Barsoum MW, Gogotsi Y. Ten Years of Progress in the Synthesis and Development of MXenes. Adv Mater. 2021;33:10.

[11] Tan TL, Jin HM, Sullivan MB, Anasori B, Gogotsi Y. High-Throughput Survey of Ordering Configurations in MXene Alloys Across Compositions and Temperatures. ACS Nano. 2017;11:4407-18.
[12] Khazaei M, Ranjbar A, Arai M, Sasaki T, Yunoki S. Electronic properties and applications of MXenes: a theoretical review. J Mater Chem C. 2017;5:2488-503.
[13] Zhang JZ, Kong N, Uzun S, Levitt A, Seyedin S, Lynch PA, et al. Scalable Manufacturing of Free-Standing, Strong $Ti_3C_2T_x$ MXene Films with Outstanding Conductivity. Adv Mater. 2020;32:9.
[14] Lipatov A, Goad A, Loes MJ, Vorobeva NS, Abourahma J, Gogotsi Y, et al. High electrical conductivity and breakdown current density of individual monolayer $Ti_3C_2T_x$ MXene flakes. Matter. 2021;4:1413-27.
[15] Lukatskaya MR, Kota S, Lin ZF, Zhao MQ, Shpigel N, Levi MD, et al. Ultra-high-rate pseudocapacitive energy storage in two-dimensional transition metal carbides. Nat Energy. 2017;2:6.
[16] Anasori B, Lukatskaya MR, Gogotsi Y. 2D metal carbides and nitrides (MXenes) for energy storage. Nat Rev Mater. 2017;2:17.
[17] Chaudhari NK, Jin H, Kim B, Baek DS, Joo SH, Lee K. MXene: an emerging two-dimensional material for future energy conversion and storage applications. J Mater Chem A. 2017;5:24564-79.
[18] Wang H, Wu Y, Yuan XZ, Zeng GM, Zhou J, Wang X, et al. Clay-Inspired MXene-Based Electrochemical Devices and Photo-Electrocatalyst: State-of-the-Art Progresses and Challenges. Adv Mater. 2018;30:28.
[19] Shahzad A, Rasool K, Nawaz M, Miran W, Jang J, Moztahida M, et al. Heterostructural TiO2/Ti3C2Tx (MXene) for photocatalytic degradation of antiepileptic drug carbamazepine. Chemical Engineering Journal. 2018;349:748-55.
[20] Shahzad F, Alhabeb M, Hatter CB, Anasori B, Hong SM, Koo CM, et al. Electromagnetic interference shielding with 2D transition metal carbides (MXenes). Science. 2016;353:1137-40.
[21] Iqbal A, Shahzad F, Hantanasirisakul K, Kim MK, Kwon J, Hong J, et al. Anomalous absorption of electromagnetic waves by 2D transition metal carbonitride Ti3CNTx (MXene). Science. 2020;369:446-+.
[22] Zhang T-Y, Wang H, Tong J, Zhang J, Wang X, Zeng Y. High-efficiency ultraviolet shielding and high transparency of Ti3C2Tx MXene/poly(vinyl alcohol) nanocomposite films. Compos Commun. 2022;33:101235.
[23] Pei YY, Zhang XL, Hui ZY, Zhou JY, Huang X, Sun GZ, et al. Ti3C2TX MXene for Sensing Applications: Recent Progress, Design Principles, and Future Perspectives. ACS Nano. 2021;15:3996-4017.
[24] Ho DH, Choi YY, Jo SB, Myoung JM, Cho JH. Sensing with MXenes: Progress and Prospects. Adv Mater. 2021;33:29.
[25] Hantanasirisakul K, Gogotsi Y. Electronic and Optical Properties of 2D Transition Metal Carbides and Nitrides (MXenes). Adv Mater. 2018;30.
[26] Ahmed A, Sharma S, Adak B, Hossain MM, LaChance AM, Mukhopadhyay S, et al. Two-dimensional MXenes: New frontier of wearable and flexible electronics. InfoMat. 2022;4:28.

[27] Chertopalov S, Mochalin VN. Environment-Sensitive Photoresponse of Spontaneously Partially Oxidized Ti3C2 MXene Thin Films. ACS Nano. 2018;12:6109-16.

[28] Zhan XX, Si C, Zhou J, Sun ZM. MXene and MXene-based composites: synthesis, properties and environment-related applications. Nanoscale Horiz. 2020;5:235-58.

[29] Lin H, Chen Y, Shi JL. Insights into 2D MXenes for Versatile Biomedical Applications: Current Advances and Challenges Ahead. Adv Sci. 2018;5:20.

[30] Soleymaniha M, Shahbazi MA, Rafieerad AR, Maleki A, Amiri A. Promoting Role of MXene Nanosheets in Biomedical Sciences: Therapeutic and Biosensing Innovations. Adv Healthc Mater. 2019;8:26.

[31] Papageorgiou DG, Li ZL, Liu MF, Kinloch IA, Young RJ. Mechanisms of mechanical reinforcement by graphene and carbon nanotubes in polymer nanocomposites. Nanoscale. 2020;12:2228-67.

[32] Shen X, Zheng QB, Kim JK. Rational design of two-dimensional nanofillers for polymer nanocomposites toward multifunctional applications. Prog Mater Sci. 2021;115:65.

[33] Dong M, Zhang H, Tzounis L, Santagiuliana G, Bilotti E, Papageorgiou DG. Multifunctional epoxy nanocomposites reinforced by two-dimensional materials: A review. Carbon. 2021;185:57-81.

[34] Riazi H, Nemani SK, Grady MC, Anasori B, Soroush M. Ti_3C_2 MXene-polymer nanocomposites and their applications. J Mater Chem A. 2021;9:8051-98.

[35] Gong KL, Zhou KQ, Qian XD, Shi CL, Yu B. MXene as emerging nanofillers for high-performance polymer composites: A review. Compos Pt B-Eng. 2021;217:40.

[36] Gao LF, Li C, Huang WC, Mei S, Lin H, Ou Q, et al. MXene/Polymer Membranes: Synthesis, Properties, and Emerging Applications. Chem Mat. 2020;32:1703-47.

[37] Ling Z, Ren CE, Zhao MQ, Yang J, Giammarco JM, Qiu JS, et al. Flexible and conductive MXene films and nanocomposites with high capacitance. Proc Natl Acad Sci U S A. 2014;111:16676-81.

[38] Yan H, Cai M, Li W, Fan XQ, Zhu MH. Amino-functionalized Ti3C2Tx with anti-corrosive/wear function for waterborne epoxy coating. Journal of Materials Science & Technology. 2020;54:144-59.

[39] Sun RH, Zhang HB, Liu J, Xie X, Yang R, Li Y, et al. Highly Conductive Transition Metal Carbide/Carbonitride(MXene)@polystyrene Nanocomposites Fabricated by Electrostatic Assembly for Highly Efficient Electromagnetic Interference Shielding. Adv Funct Mater. 2017;27:11.

[40] Malaki M, Varma RS. Mechanotribological Aspects of MXene-Reinforced Nanocomposites. Adv Mater. 2020;32:20.

[41] Lipatov A, Lu HD, Alhabeb M, Anasori B, Gruverman A, Gogotsi Y, et al. Elastic properties of 2D $Ti_3C_2T_x$ MXene monolayers and bilayers. Sci Adv. 2018;4:7.

[42] Lipatov A, Alhabeb M, Lu HD, Zhao SS, Loes MJ, Vorobeva NS, et al. Electrical and Elastic Properties of Individual Single-Layer $Nb_4C_3T_x$ MXene Flakes. Adv Electron Mater. 2020;6:10.

[43] Borysiuk VN, Mochalin VN, Gogotsi Y. Molecular dynamic study of the mechanical properties of two-dimensional titanium carbides $Ti_{n+1}C_n$ (MXenes). Nanotechnology. 2015;26:10.

[44] Hu T, Yang J, Li W, Wang X, Li CM. Quantifying the rigidity of 2D carbides (MXenes). Phys Chem Chem Phys. 2020;22:2115-21.

[45] Liu L, Ying G, Wen D, Zhang K, Hu C, Zheng Y, et al. Aqueous solution-processed MXene ($Ti_3C_2T_x$) for non-hydrophilic epoxy resin-based composites with enhanced mechanical and physical properties. Mater Des. 2021;197:109276.

[46] Wazalwar R, Tripathi M, Raichur AM. Curing Behavior and Mechanical Properties of Tetra-Functional Epoxy Reinforced with Polyethyleneimine-Functionalized MXene. ACS Appl Polym Mater. 2022;4:2573-84.

[47] Zhang H, Wang LB, Chen Q, Li P, Zhou AG, Cao XX, et al. Preparation, mechanical and anti-friction performance of MXene/polymer composites. Mater Des. 2016;92:682-9.

[48] Sheng XX, Zhao YF, Zhang L, Lu X. Properties of two-dimensional Ti_3C_2 MXene/thermoplastic polyurethane nanocomposites with effective reinforcement via melt blending. Compos Sci Technol. 2019;181:8.

[49] Zhi WQ, Xiang SL, Bian RJ, Lin RZ, Wu KH, Wang TW, et al. Study of MXene-filled polyurethane nanocomposites prepared via an emulsion method. Compos Sci Technol. 2018;168:404-11.

[50] Luo JQ, Zhao S, Zhang HB, Deng ZM, Li LL, Yu ZZ. Flexible, stretchable and electrically conductive MXene/natural rubber nanocomposite films for efficient electromagnetic interference shielding. Compos Sci Technol. 2019;182:8.

[51] Papageorgiou DG, Kinloch IA, Young RJ. Mechanical properties of graphene and graphene-based nanocomposites. Prog Mater Sci. 2017;90:75-127.

[52] Young RJ, Liu MF, Kinloch IA, Li SH, Zhao X, Valles C, et al. The mechanics of reinforcement of polymers by graphene nanoplatelets. Compos Sci Technol. 2018;154:110-6.

[53] Mohiuddin TMG, Lombardo A, Nair RR, Bonetti A, Savini G, Jalil R, et al. Uniaxial strain in graphene by Raman spectroscopy: G peak splitting, Gruneisen parameters, and sample orientation. Phys Rev B. 2009;79:8.

[54] Deng LB, Eichhorn SJ, Kao CC, Young RJ. The Effective Young's Modulus of Carbon Nanotubes in Composites. ACS Appl Mater Interfaces. 2011;3:433-40.

[55] Li ZL, Young RJ, Kinloch IA. Interfacial Stress Transfer in Graphene Oxide Nanocomposites. ACS Appl Mater Interfaces. 2013;5:456-63.

[56] Wang F, Li SH, Bissett MA, Kinloch IA, Li ZL, Young RJ. Strain engineering in monolayer WS(2)and WS(2)nanocomposites. 2D Mater. 2020;7:13.

[57] Wang WM, Li ZL, Marsden AJ, Bissett MA, Young RJ. Mechanisms of reinforcement of PVA-Based nanocomposites by hBN nanosheets. Compos Sci Technol. 2022;218:8.

[58] Liu M, Zhuo Y, Sarycheva A, Gogotsi Y, Bissett MA, Young RJ, et al. Deformation of and Interfacial Stress Transfer in Ti3C2 MXene–Polymer Composites. ACS Appl Mater Interfaces. 2022;14:10681-90.

[59] Alhabeb M, Maleski K, Anasori B, Lelyukh P, Clark L, Sin S, et al. Guidelines for Synthesis and Processing of Two-Dimensional Titanium Carbide (Ti3C2TX MXene). Chem Mat. 2017;29:7633-44.
[60] Sarycheva A, Gogotsi Y. Raman Spectroscopy Analysis of the Structure and Surface Chemistry of Ti3C2Tx MXene. Chem Mat. 2020;32:3480-8.
[61] Lipatov A, Alhabeb M, Lukatskaya MR, Boson A, Gogotsi Y, Sinitskii A. Effect of Synthesis on Quality, Electronic Properties and Environmental Stability of Individual Monolayer Ti3C2 MXene Flakes. Adv Electron Mater. 2016;2:9.
[62] Kiran NU, Deore AB, More MA, Late DJ, Rout CS, Mane P, et al. Comparative Study of Cold Electron Emission from 2D $Ti_3C_2T_x$ MXene Nanosheets with Respect to Its Precursor Ti_3SiC_2 MAX Phase. ACS Appl Electron Mater. 2022;4:2656-66.
[63] Gupta S, Pramanik AK, Kailath A, Mishra T, Guha A, Nayar S, et al. Composition dependent structural modulations in transparent poly(vinyl alcohol) hydrogels. Colloid Surf B-Biointerfaces. 2009;74:186-90.
[64] Hu T, Wang J, Zhang H, Li Z, Hu M, Wang X. Vibrational properties of Ti3C2 and Ti3C2T2 (T = O, F, OH) monosheets by first-principles calculations: a comparative study. Phys Chem Chem Phys. 2015;17:9997-10003.
[65] Li ZL, Young RJ, Wilson NR, Kinloch IA, Valles C, Li Z. Effect of the orientation of graphene-based nanoplatelets upon the Young's modulus of nanocomposites. Compos Sci Technol. 2016;123:125-33.
[66] Liu MF, Papageorgiou DG, Li SH, Lin KL, Kinloch IA, Young RJ. Micromechanics of reinforcement of a graphene-based thermoplastic elastomer nanocomposite. Compos Pt A-Appl Sci Manuf. 2018;110:84-92.
[67] Li ZL, Young RJ, Kinloch IA, Wilson NR, Marsden AJ, Raju APA. Quantitative determination of the spatial orientation of graphene by polarized Raman spectroscopy. Carbon. 2015;88:215-24.
[68] Papageorgiou DG, Kinloch IA, Young RJ. Hybrid multifunctional graphene/glass-fibre polypropylene composites. Compos Sci Technol. 2016;137:44-51.
[69] Young RJ, Lovell PA. Introduction to Polymers, Third Edition: Taylor & Francis; 2011.

Declaration of interests

☒ The authors declare that they have no known competing financial interests or personal relationships that could have appeared to influence the work reported in this paper.

☐ The authors declare the following financial interests/personal relationships which may be considered as potential competing interests: